Supporting Information

Alleviating the Volume Expansion of Silicon Anodes by Constructing High-Strength Ordered Multidimensional Encapsulation Structure

Synthesis of Ester-Modified SiQDs

In a glove box, 40 mL of diglycol solution and 200 μL of silicon tetrachloride were mixed and stirred for 10 minutes. The solution was transferred to a polytetrafluoroethylene-lined vessel and reacted at 160°C for 6 hours. After cooling, it was dialyzed (3000 Da cutoff) in a glove box for 24 hours and filtered to obtain SiQDs. To modify their surface, 0.3 g of citric acid ester was added, stirred for 1.5 hours, centrifuged, and freeze-dried to yield ester-modified silicon quantum dots.
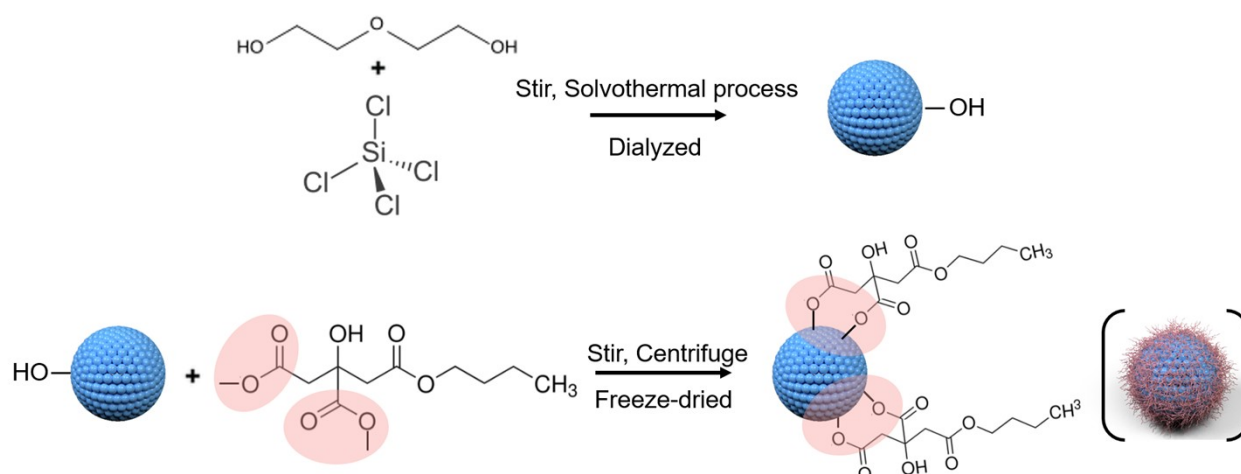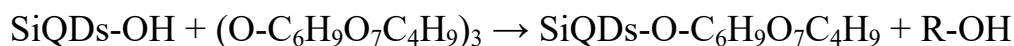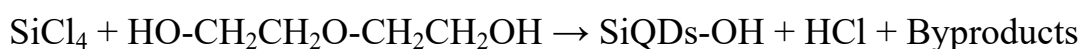

Figure S1. Schematic illustration for the formation mechanism of ester-modified SiQDs.

The general reaction process can be represented as:

$$SiCl_4 + HO\text{-}CH_2CH_2O\text{-}CH_2CH_2OH \rightarrow SiQDs\text{-}OH + HCl + Byproducts$$

$$SiQDs\text{-}OH + (O\text{-}C_6H_9O_7C_4H_9)_3 \rightarrow SiQDs\text{-}O\text{-}C_6H_9O_7C_4H_9 + R\text{-}OH$$

Diglycol acts as both a reducing agent and stabilizer, reducing $SiCl_4$ to silicon and forming silicon quantum dots. Hydrogen chloride (HCl) is the main byproduct of the reaction. The hydroxyl group (-OH) on the SiQDs attacks the carbonyl carbon of the ester group, breaking the ester bond and forming a new Si-O bond.

Synthesis of COS

0.15 g hydroquinone and 30 mL ammonia solution (prepared by dissolving 10 mL of ammonia solution in 500 mL of water) were stirred in a flask for 0.5 hours. 0.3 mL formaldehyde was added and stirred for 1 hour. 0.3 g ester-modified silicon quantum dots were added and stirred for 12 hours at 80°C under nitrogen. After repeated centrifugation, washed and dried for 12 h at 70 °C in a vacuum oven. COS precursor was placed in a tube furnace, and the temperature was increased to 300°C at a rate of 5°C min^{-1} and held for 2 hours under a protective atmosphere. Subsequently, the temperature was further increased to 600°C at the same rate and maintained for 8 hours. The black product obtained after cooling was designated as COS.
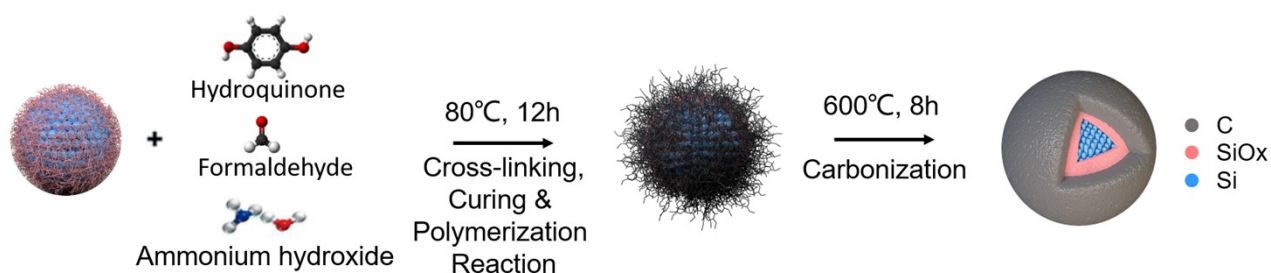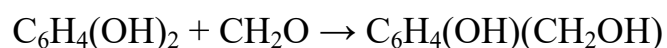

Figure S2. Schematic illustration for the formation mechanism of COS.

The chemical reaction process can be represented as:
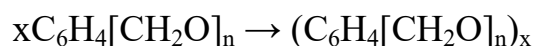
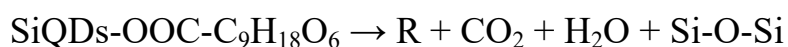1. Condensation Reaction

- Formation of Hydroxymethyl Resorcinol
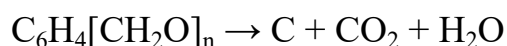
$$C_6H_4(OH)_2 + CH_2O \rightarrow C_6H_4(OH)(CH_2OH)$$

- Polymerization to Form Phenolic Resin

$$C_6H_4(OH)(CH_2OH) + nCH_2O \rightarrow C_6H_4(OH)[CH_2O]_n$$

- Curing Reaction

$$xC_6H_4[CH_2O]_n \rightarrow (C_6H_4[CH_2O]_n)_x$$

2. Carbonization Reaction

$$C_6H_4[CH_2O]_n \rightarrow C + CO_2 + H_2O$$

$$SiQDs\text{-}OOC\text{-}C_9H_{18}O_6 \rightarrow R + CO_2 + H_2O + Si\text{-}O\text{-}Si$$

High-temperature treatment to produce a carbon material with the desired porous structure. During the carbonization process, the citrate ester undergoes thermal decomposition, converting its alkyl chains into carbon. The remaining O atoms then react with Si to form SiO_x, resulting in the in situ formation of a SiO_x layer on the surface of the SiQDs.

Synthesis of CCOS

20 mL of phenolic resin solution was mixed with EtOH at a volume ratio of 7:1 and stirred for 0.5 hours at 25 °C. After adding 0.4g COS sample, the mixture was stirred for an additional 2 hours. This mixture was then transferred to a polytetrafluoroethylene-lined high-pressure vessel and heated at 180°C for 4 hours to solidify, forming PF-EtOH. The resulting product was dried at 120°C under vacuum for 12 hours, and placed in a tube furnace. The temperature was increased to 400°C at 2°C min^{-1} and held for 60 minutes, then further increased to 700°C at 5°C min^{-1} and held for 5 hours in Ar. The black product obtained after cooling was designated as CCOS.
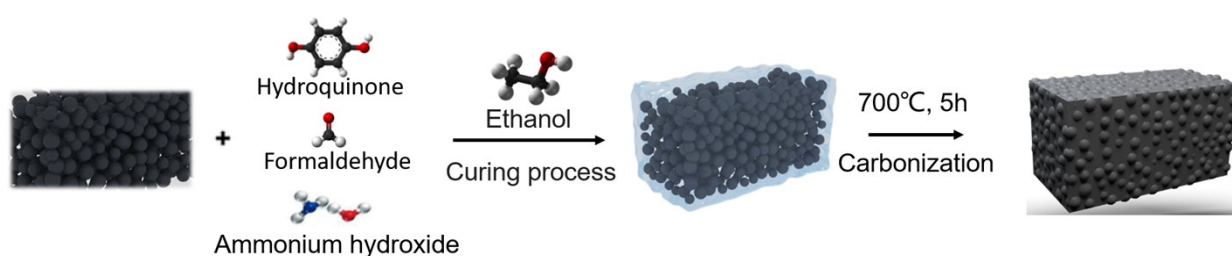

Figure S3. Schematic illustration for the formation mechanism of CCOS.

Before curing, ethanol is mixed with the phenolic resin. Ethanol acts as a pore-

forming agent, creating pores during the curing process, which involves heating the phenolic resin. As the ethanol evaporates under heat, it generates bubbles within the resin, which subsequently form pores. Concurrently, the phenolic polymer network undergoes cross-linking, resulting in a three-dimensional structure. The evaporation of ethanol and the formation of bubbles lead to the creation of closed pores within the resin. Following the curing process, the material is carbonized by heating it to elevated temperatures. During carbonization, the organic groups are eliminated, and the cured resin is transformed into a carbon material. The pores formed during curing are preserved, yielding a carbon layer with closed pores.

Material characterization

The X-ray diffraction (XRD) was performed using a Rigaku X-ray diffractometer with Cu Kα radiation ($\lambda = 1.5418$ Å) at a scanning rate of $2°$ min^{-1} to determine the crystal phases. The morphological features were examined using a scanning electron microscope (SEM, Nova NanoSEM-23) equipped with an energy dispersive spectrometer (EDS, Oxford-Instruments), while the microstructural details were observed with a high-resolution transmission electron microscope (HRTEM). Raman spectra were acquired on an HR-800 spectrometer (Jobin-Yvon LabRAM) using a 514 nm laser excitation, covering the range of 200-3500 cm^{-1}. The carbon content of the sample was determined by thermogravimetric analysis (TG, 209 F3 Tarsus). The BET (Brunauer-Emmett-Teller) specific surface areas were calculated from nitrogen adsorption results, measured on a Tristar-3020 instrument at 77 K. Before measurement,

all samples were degassed at 180°C for 5 hours. Fourier Transformed Infrared Spectroscopy (FT-IR) was carried out on Thermo Scientific Nicolet 6700.

Electrochemical Measurements

The working electrodes were prepared as follows: active materials (CCOS, SiNPs) were mixed with conductive carbon black (CB) and sodium carboxymethylcellulose (CMC) in a weight ratio of 7:1:2 to form homogeneous slurries with DI water. These slurries were then cast onto copper foil and dried in a vacuum oven at 80°C for 24 hours. Electrodes were cut into 12 mm diameter sheets with an active material loading ranging from approximately 0.6 mg cm^{-2}. The SiNPs were purchased from Aladdin without further processing. The specifications of the silicon nanoparticles are 99.9% metals basis purity and, 20-60 nm size range. For electrochemical tests, half cells (2032 coin cells) were assembled in an Ar-filled glove box with lithium metal as the reference electrode and Celgard 2500 membrane as the separator. The electrolyte contained 1 M lithium hexafluorophosphate (LiPF$_6$) dissolved in a mixture of ethylene carbonate (EC), diethyl carbonate (DEC), and ethyl methyl carbonate (EMC) in a 1:1:1 volume ratio, with the addition of 5 wt% FEC. Galvanostatic charge/discharge testing was conducted at 25°C using a LAND 2001CT battery tester, with a voltage range of 0.01-3.0 V and various current densities. The galvanostatic intermittent titration technique (GITT) was performed within the same voltage range. Additionally, CV curves and electrochemical impedance spectra (EIS) were obtained using a BioLogic SP-300 electrochemical workstation.
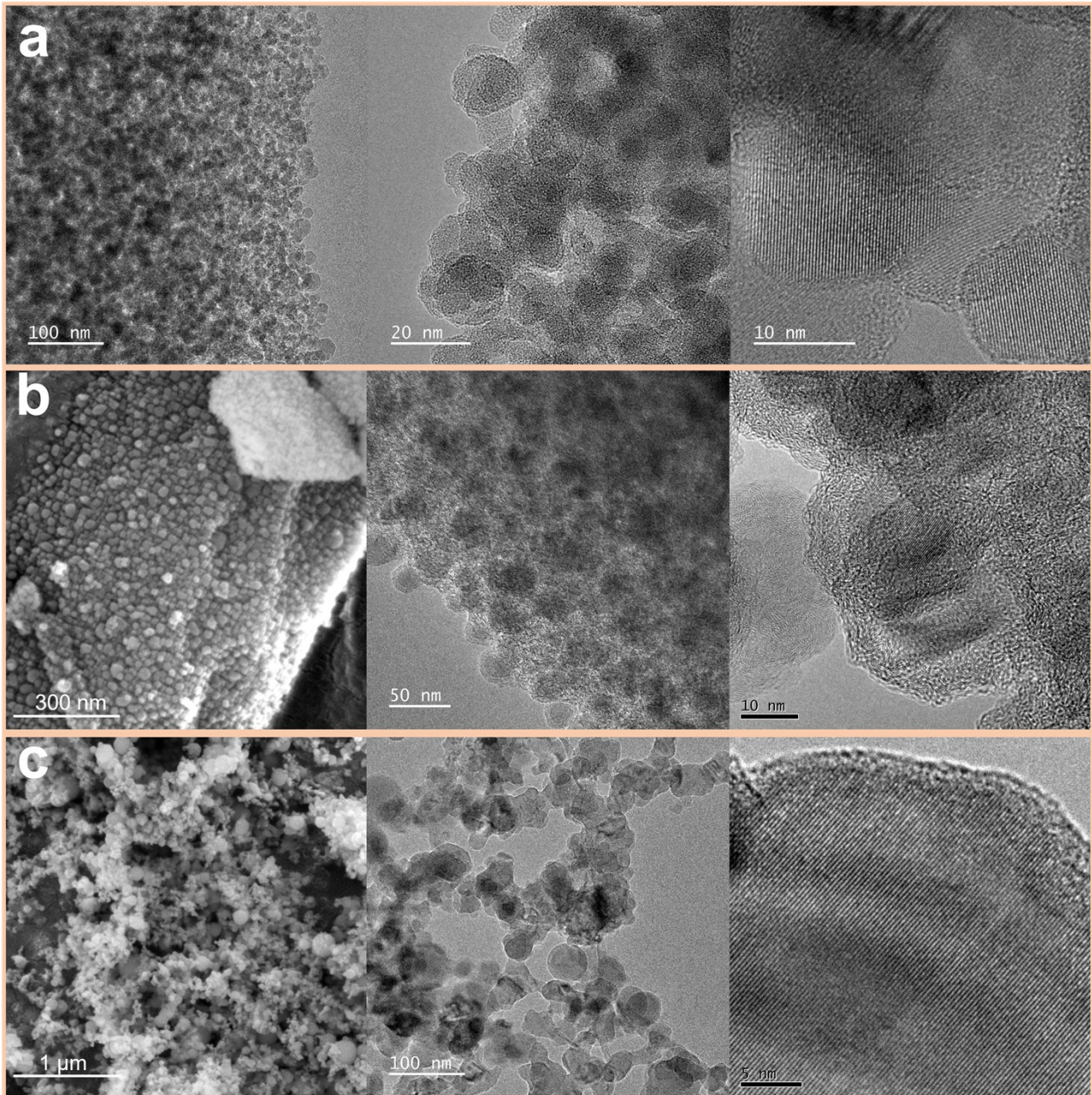
Figure S4. (a) TEM image and HRTEM image of SiQDs. (b) SEM, TEM and HRTEM images of COS. (c) SEM, TEM and HRTEM images of SiNPs.
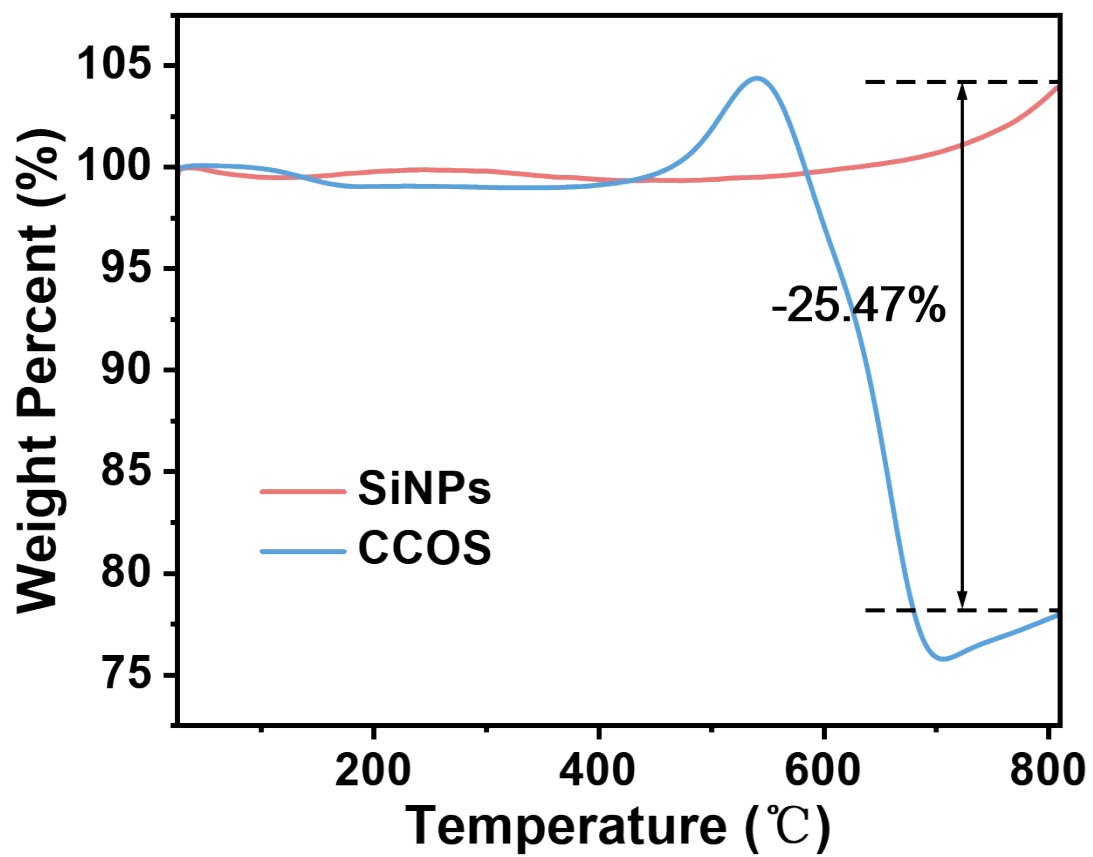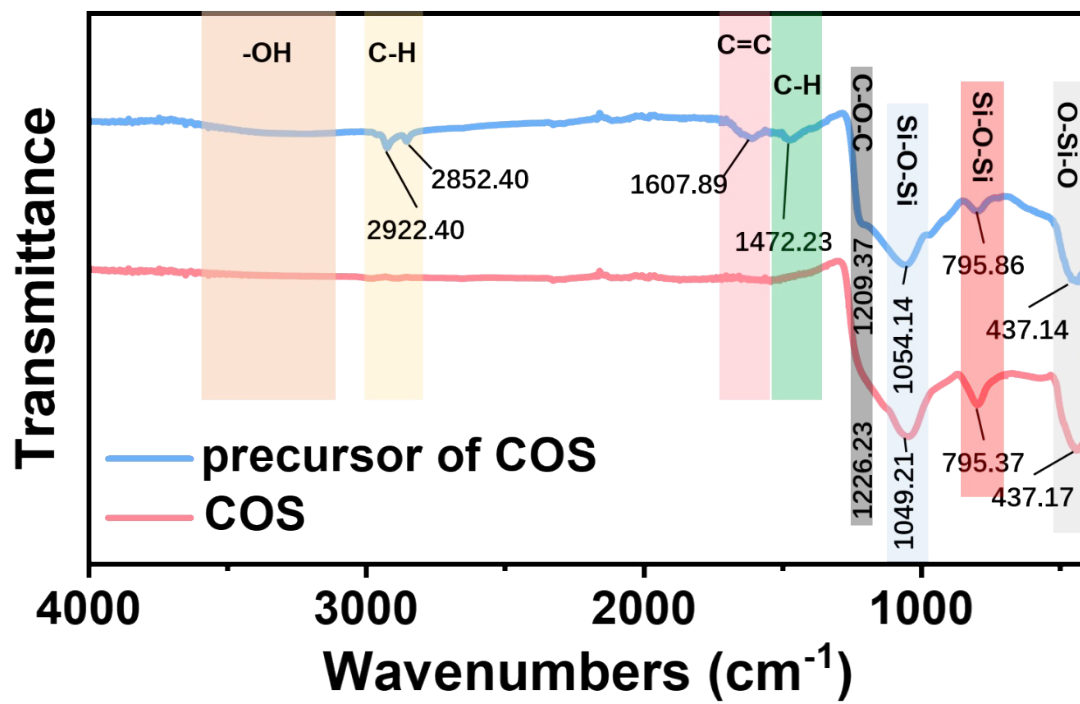
Figure S5. TGA curves of CCOS and SiNPs

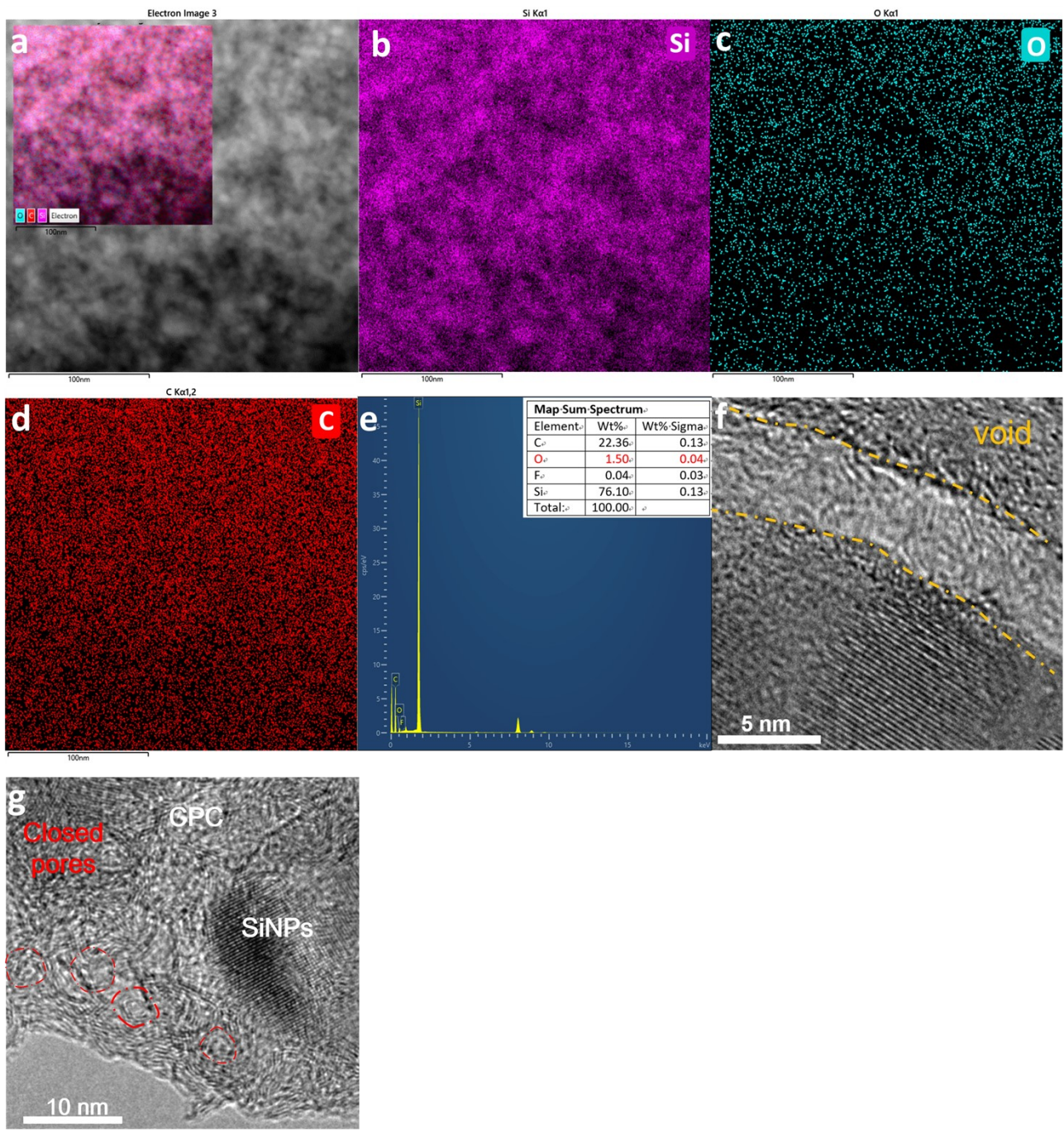Figure S6. FTIR spectra of COS before and after carbonization.

Figure S7. (a) TEM image and (input) electron image. TEM-based EDS mapping of (b) Si, (c) O, (d) C, and (e) map sum spectrum. (f) TEM image of the CCOS after etching. (g) TEM image of the closed pores in the CPC layer.
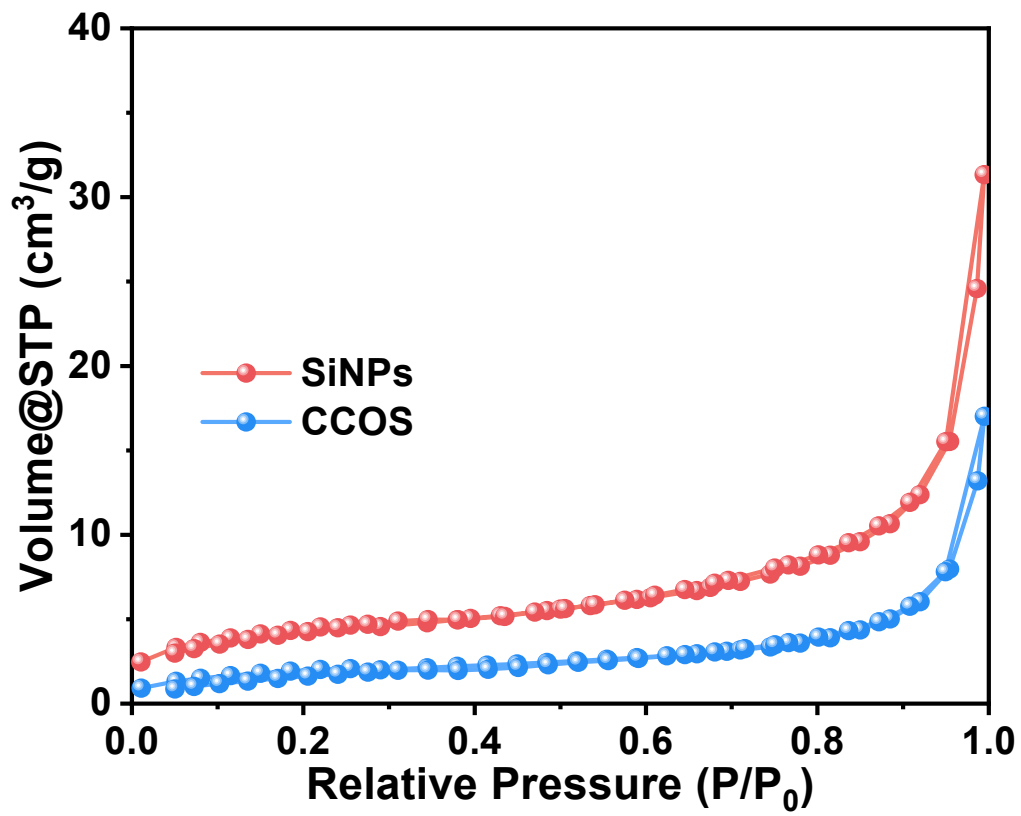
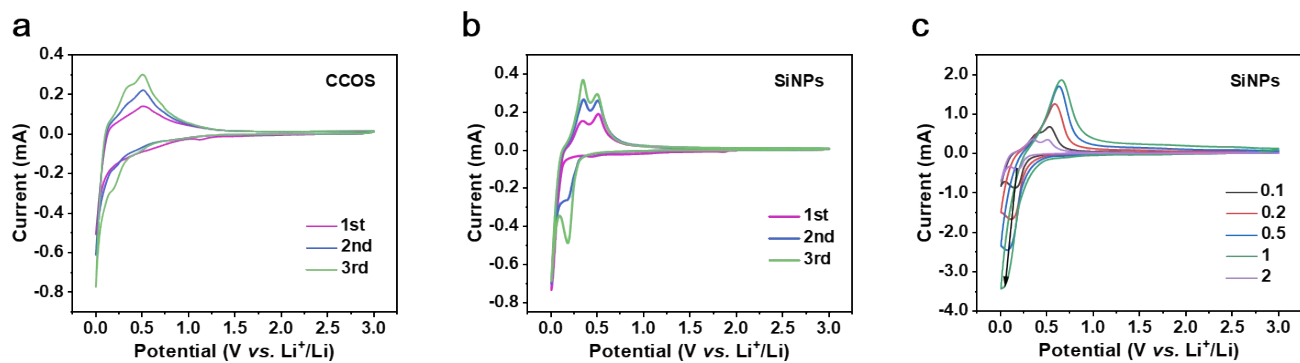Figure S8. Nitrogen adsorption/desorption isotherms of CCOS and SiNPs

Figure S9. Typical CV plots during the initial three cycles at 0.1 mV s-1 for (a) CCOS and (b) SiNPs. (c) The CV curves at different sweep rates of SiNPs.
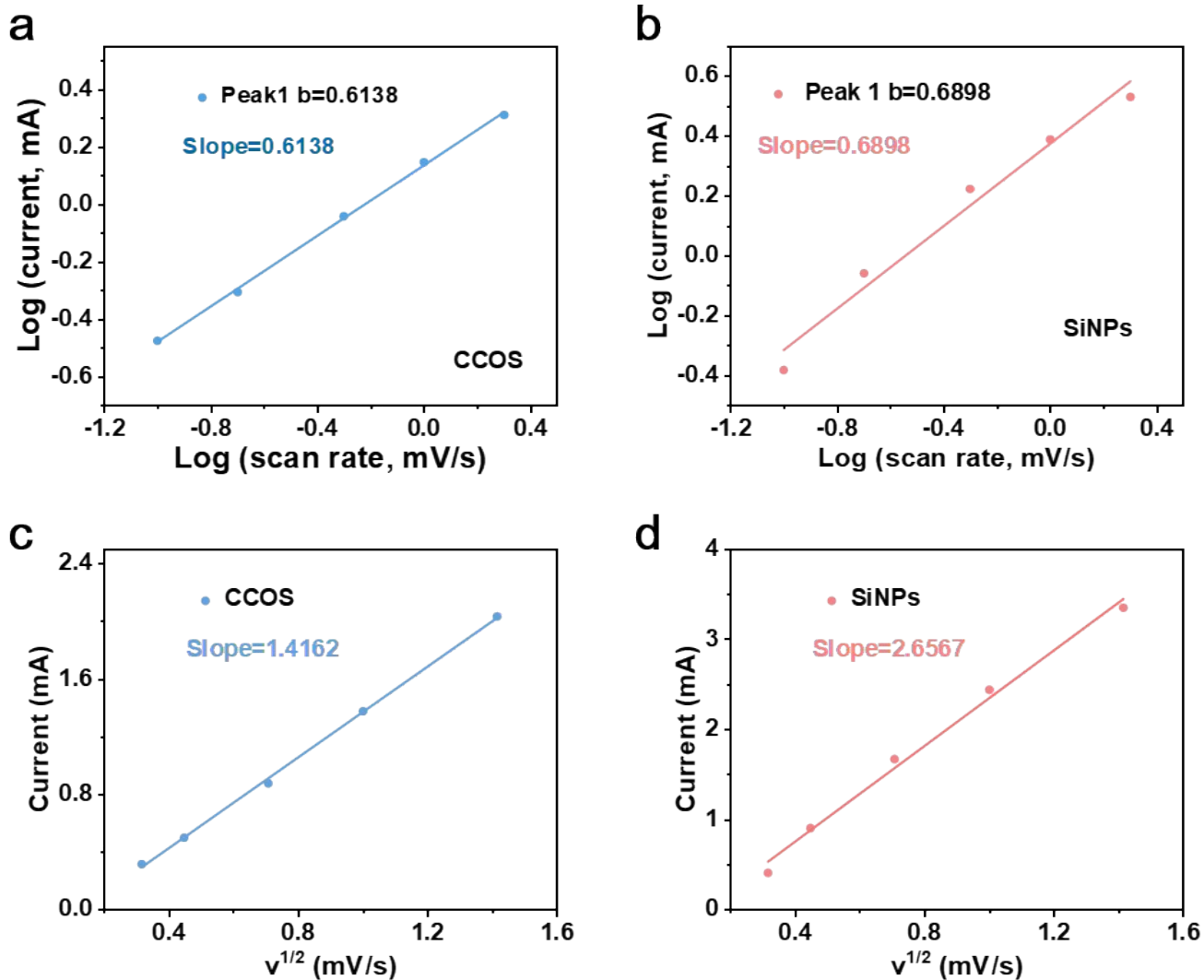
Figure S10. The plots of log(i) vs log(v) calculated from CV curves of (a) CCOS and (b) SiNPs. The relative electrochemically active surface area of (c) CCOS and (d) SiNPs.
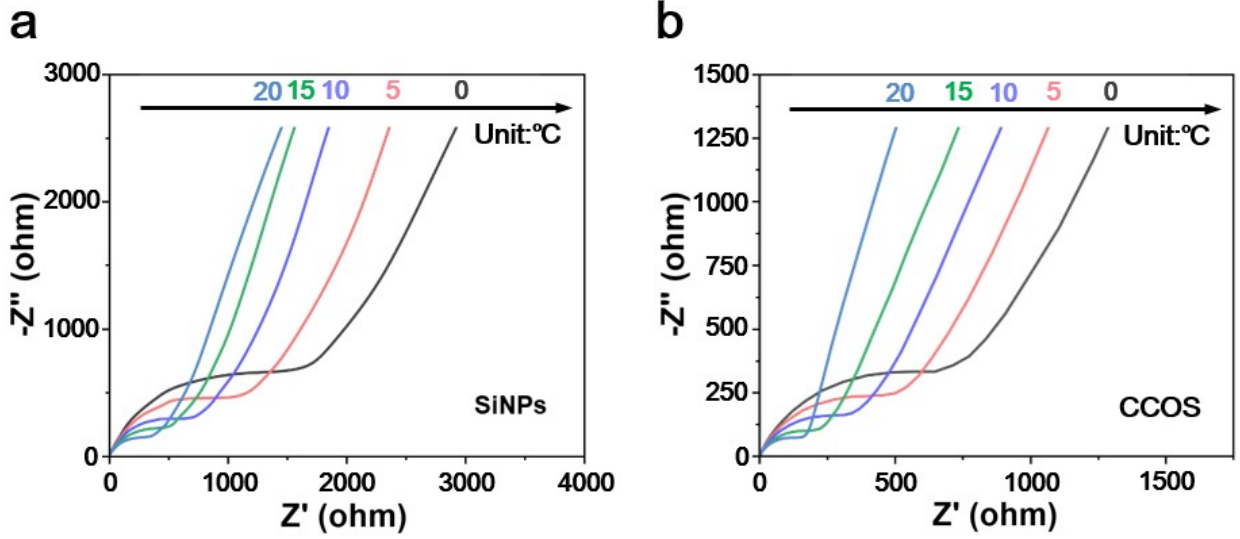
Figure S11. Nyquist curves at different operating temperatures from 0 to 25 °C for (a) SiNPs, and (b) CCOS.
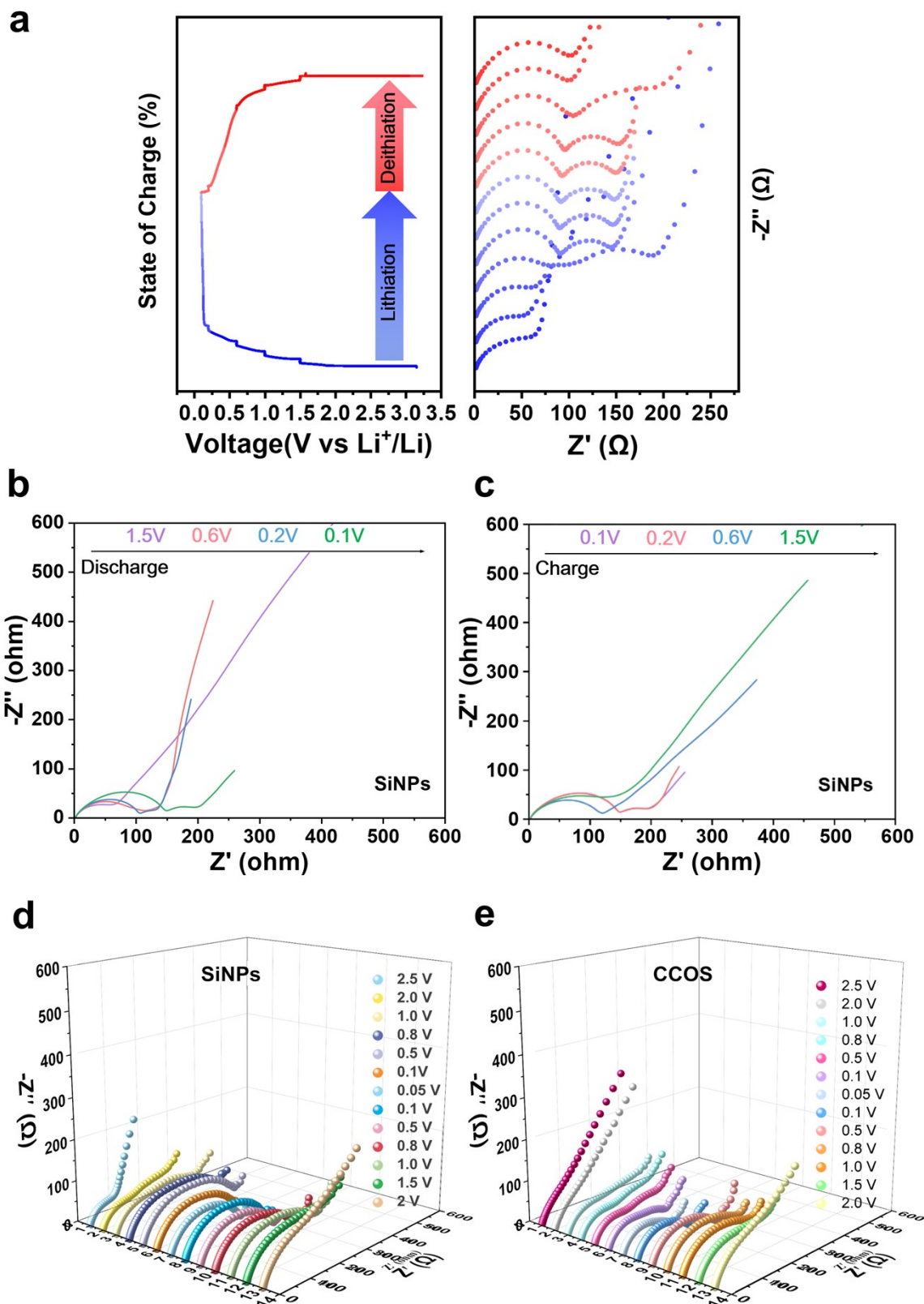
Figure S12. (a) In-situ EIS Nyquist plots of CCOS calculated at selected potential during the initial cycle. In-situ EIS Nyquist plots of SiNPs calculated at selected potential during the initial cycle, Discharge (b) and Charge (c). In-situ EIS Nyquist plots at selected potential during the high rate (5.0 A g^{-1}) cycling of (d) SiNPs and (e) CCOS.

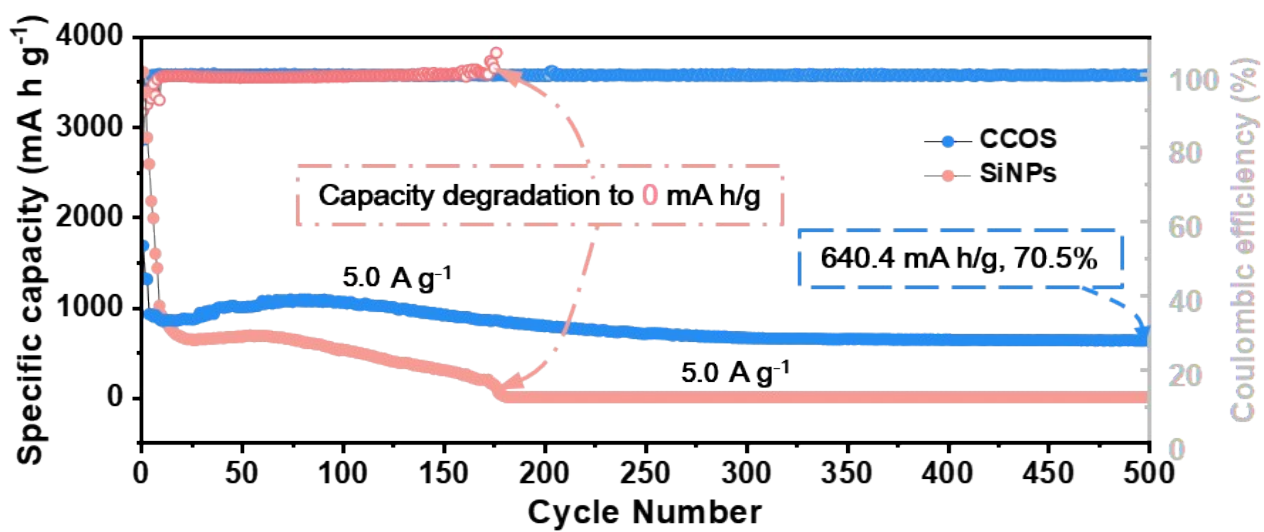Figure S13. Long cycle performance at 5 A g^{-1} rate in half-cell for CCOS and SiNPs.
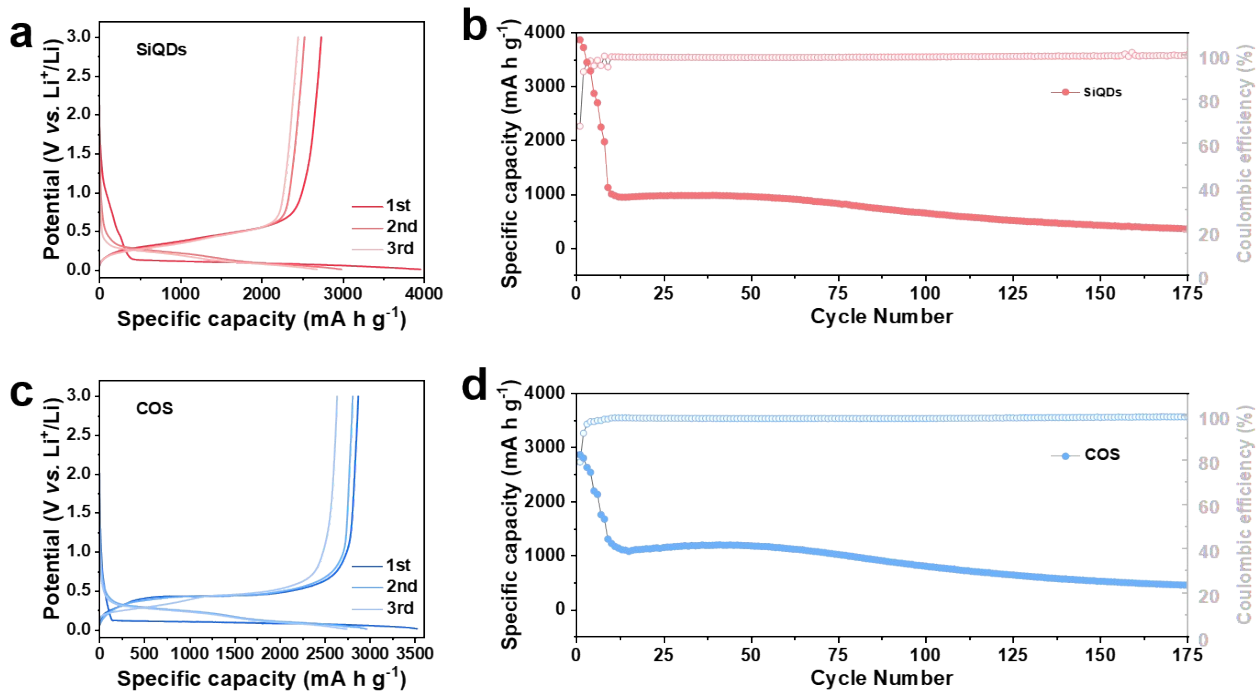
Figure S14. (a) Initial discharge/charge curves and (b) long cycle performance of SiQDs. (c) Initial discharge/charge curves and (d) long cycle performance of COS.
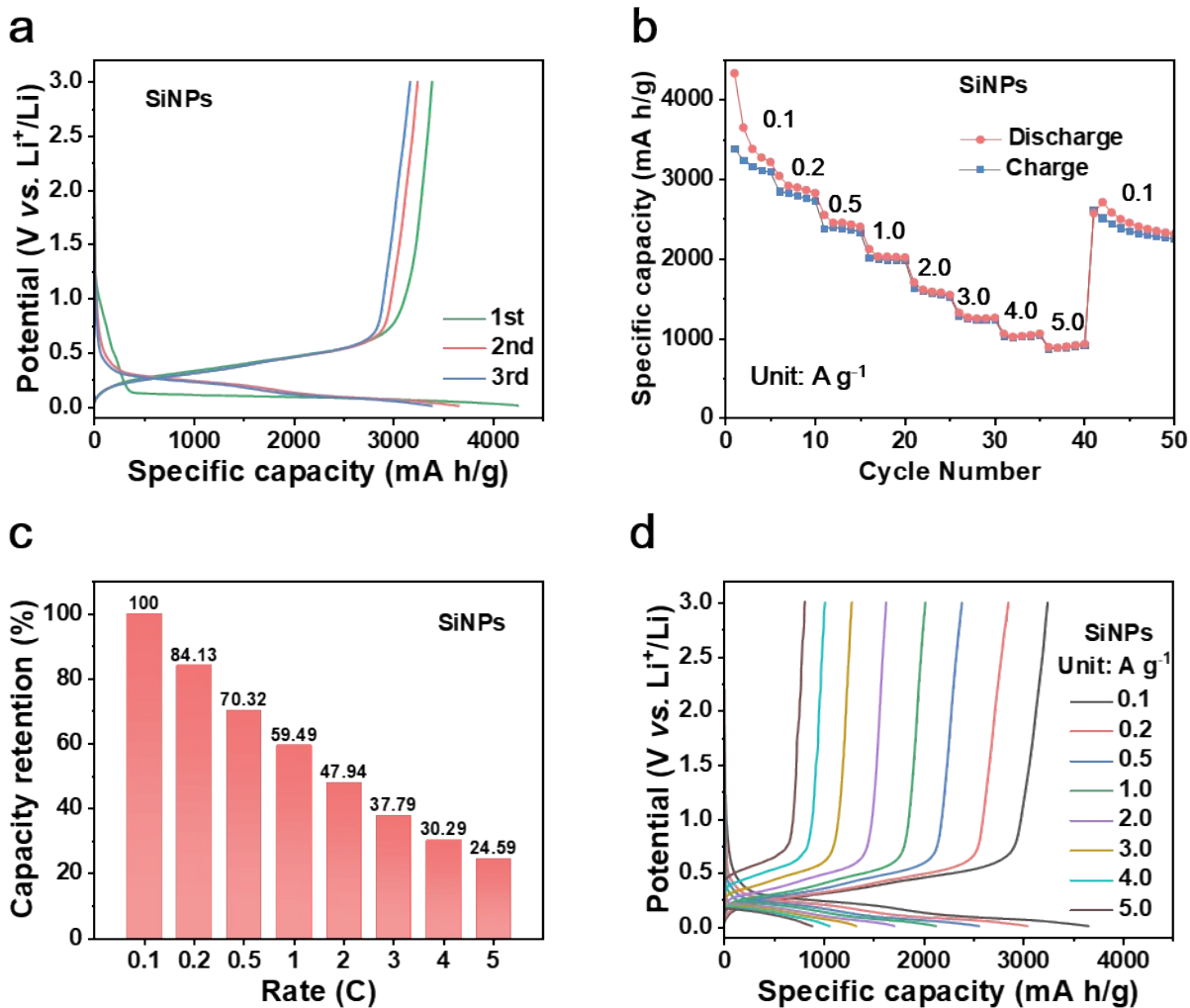
Figure S15. (a) Initial discharge/charge curves. (b) Rate performances of SiNPs. (c) Capacity retention at different discharge rates of SiNPs. (d) (Dis)charge curves of SiNPs at different rates.
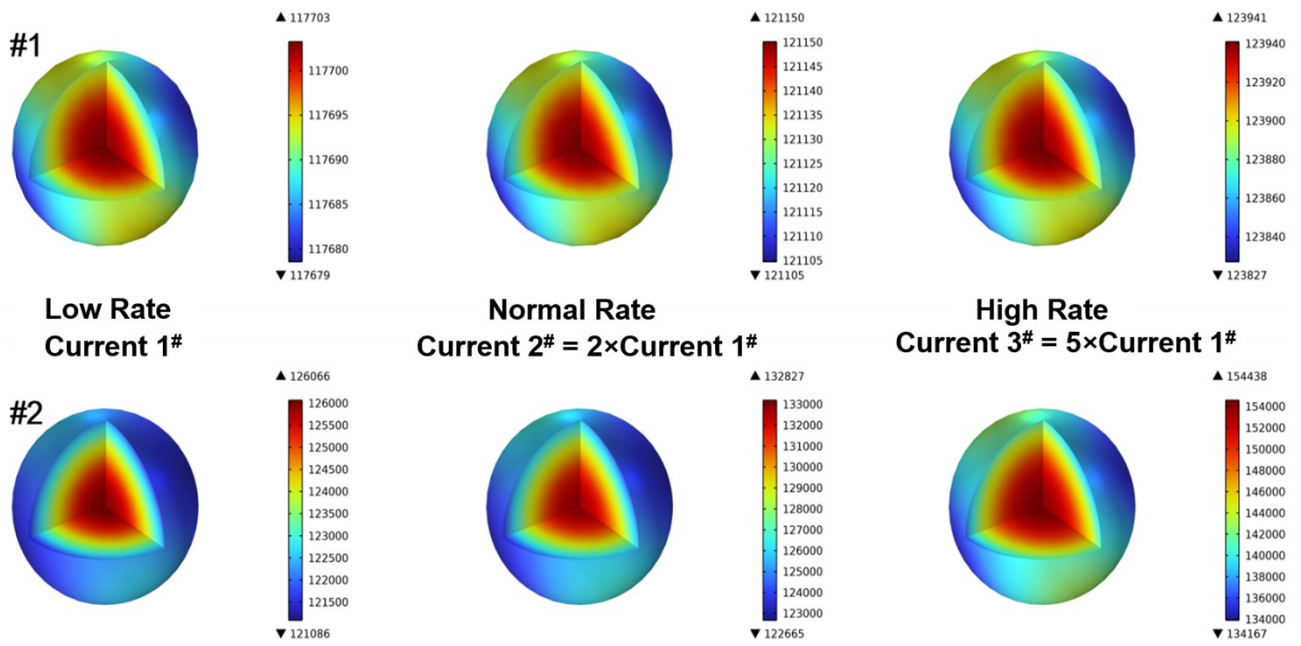
Figure S16. COMSOL simulation diagrams of the Li$^+$ concentration distribution of SiQDs (#1) and SiNPs (#2) during delithiation process.
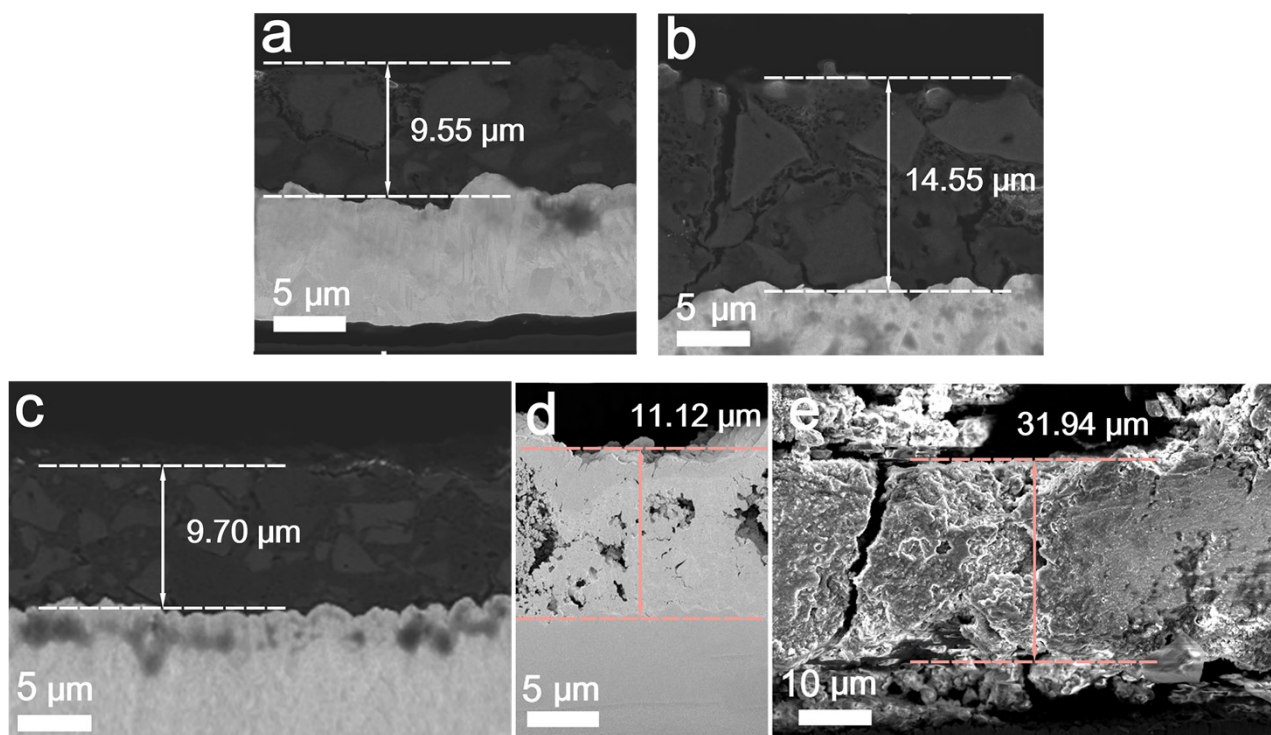
Figure S17. Cross-sections of the electrodes of CCOS after 100 cycles at (a) 0.5 Ag⁻¹ and (b) 3.0 Ag⁻¹. (c) After 50 cycles at 1.0 Ag⁻¹. (d) Cross-sections of the electrodes of SiNPs before cycles, (e) after 500 cycles at 1.0 Ag⁻¹.

After approximately estimating, the electrode expansion rates after 500 cycles were 103.4% for the CCOS electrode at 5 A g^{-1} and 187.24% for the SiNPs electrode at 1 A g^{-1}.

$$Expansion\ rate = \frac{d_A - d_0}{d_0} \times 100\%$$

Where d_0 is the thickness of the electrode before cycling. d_A is the thickness of the electrode after cycling.
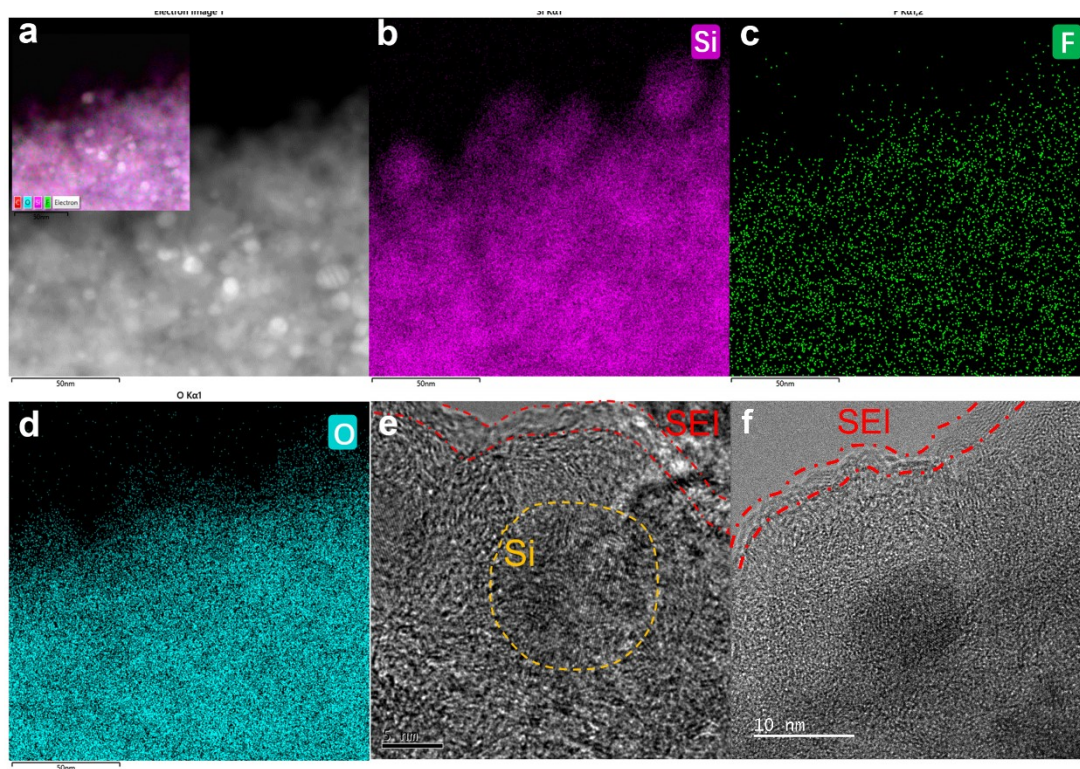
Figure S18. (a) TEM image and (in-put) electron image. TEM-based EDS mapping of (b) Si, (c) F, (d) O. (e, f) TEM images of CCOS for SEI film.
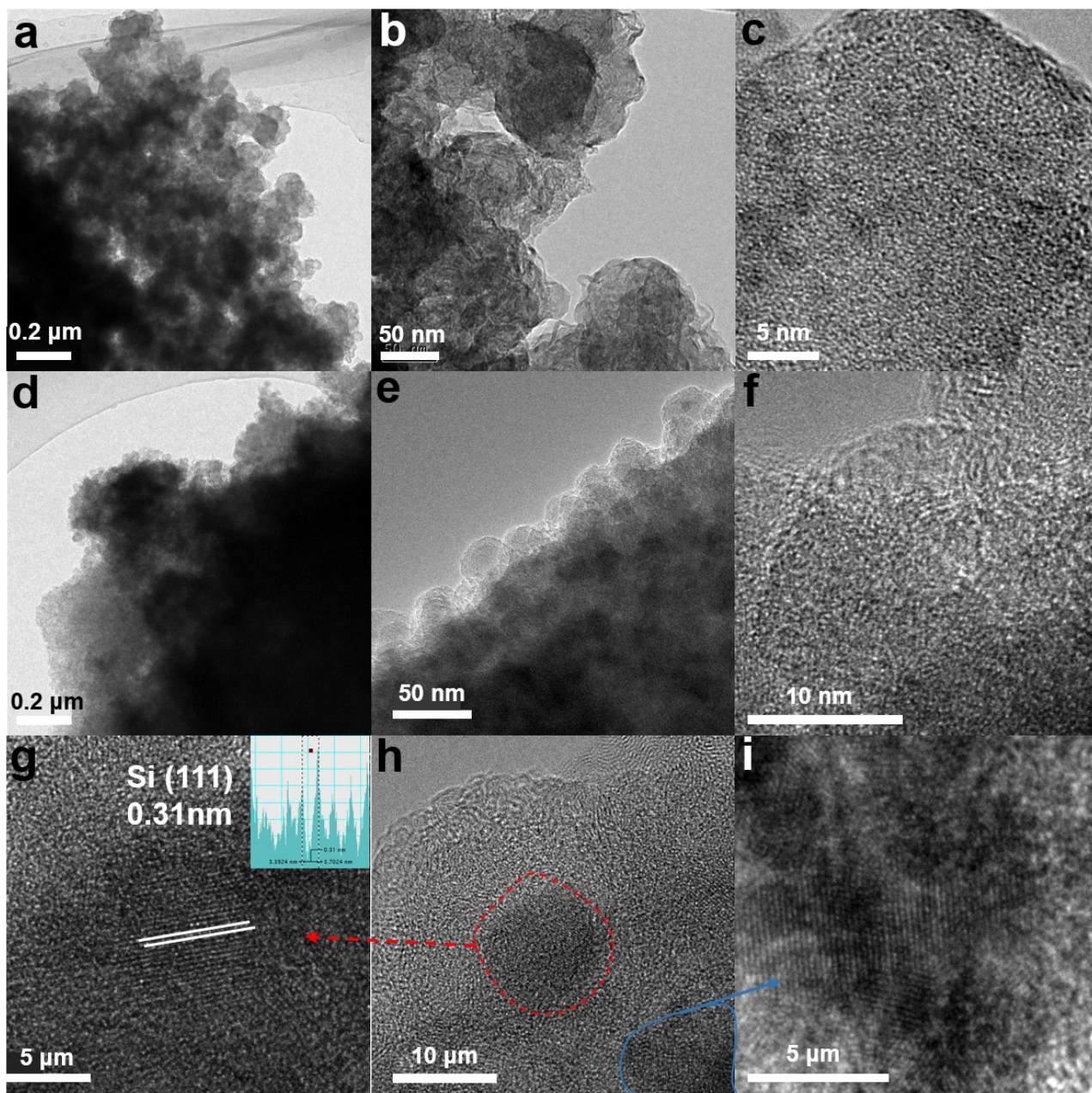
Figure S19. (a, b) TEM images and (c) HRTEM image of SiNPs after complete delithiation (open circuit voltage > 3.0 V) at 1.0 A g^{-1} for 100 cycles.. (d, e) TEM images and (f) HRTEM image of CCOS during lithiation (open circuit voltage < 50 mV). (g, h, i) HRTEM images of CCOS after complete delithiation (open circuit voltage > 3.0 V) at 1.0 A g^{-1} for 100 cycles.
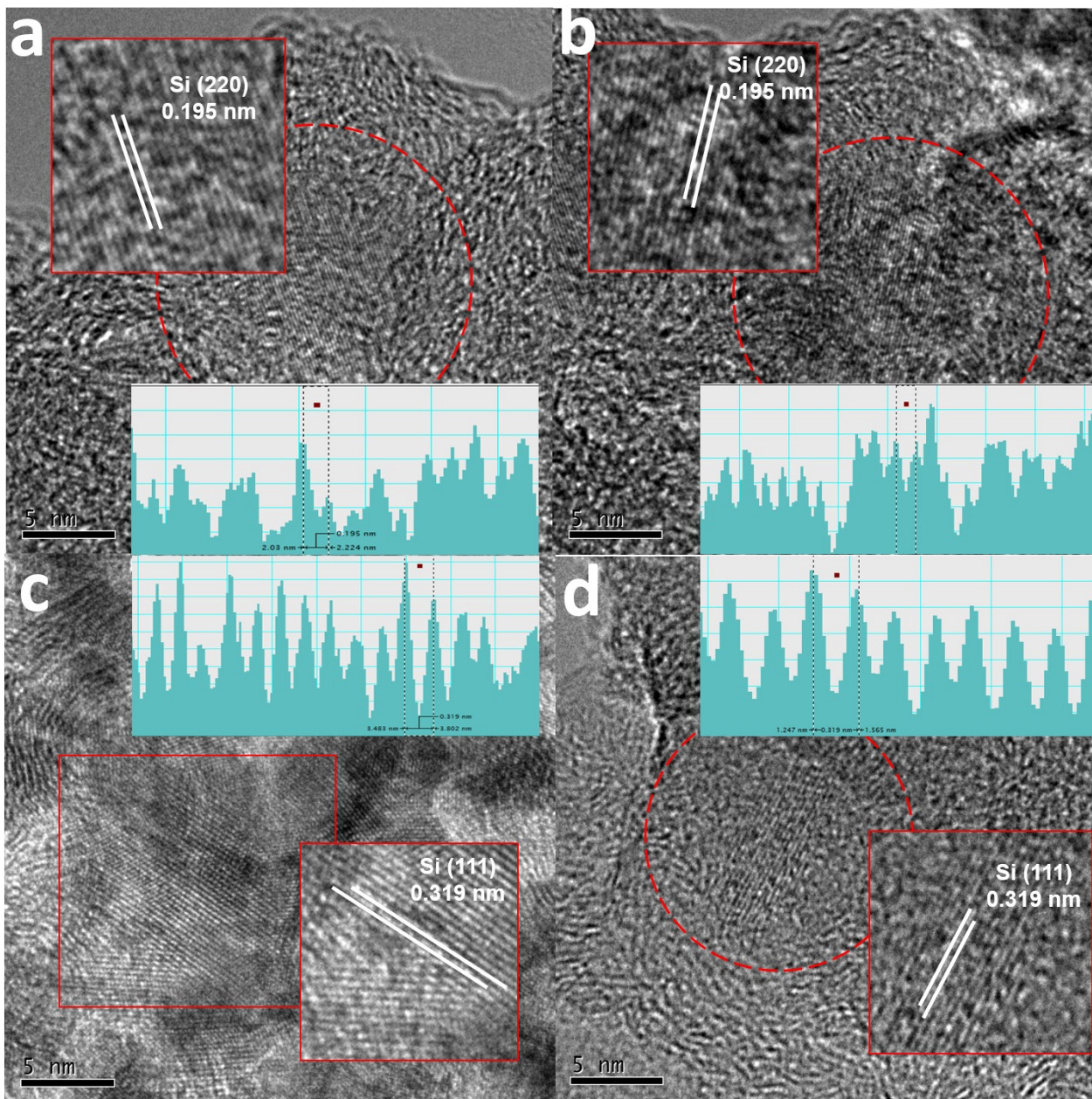
Figure S20. TEM and HRTEM images of CCOS after (a,b) 300 cycles at 1.0 A g^{-1}, (c,d) 500 cycles at 5.0 A g^{-1}.

Numerical Simulations:

Supplementary Note 1:

The value of b can be decided follows the equation:

$$i = av^b$$

$$log(i) = blog(v) + log(a)$$

Where i is the current and v is the sweep rate. The value of b can be determined by calculating the slope of the log(i) versus log(v) curves. A b value of 1 indicates a pseudocapacitive contribution, while a b value of 0.5 signifies an ionic diffusion-controlled reaction.

The specific contribution ratio of diffusion control ($k_2v^{1/2}$) and the pseudocapacitance control (k_1v) can be calculated according to the following formula:

$$i\,(V) = k_1v + k_2v^{1/2}$$

The constants of k_1 and k_2 are obtained by this equation.[9]

Supplementary Note 2

The relative electrochemical active surface area was evaluated by analyzing the relationship between the scan rate and peak current, as described by the Randles-Sevcik equation.

$$Ip = (2.69 \times 10^5)n^{3/2}ACD^{1/2}v^{1/2}$$

Where I_P is peak current. n, the number of electrons transferred. A, the active surface area. D, the diffusion coefficient of lithium ion. $C0$, the bulk concentration of lithium ion. v, the scan rates.[10]

Supplementary Note 3

The value of D_{Li^+} can be calculated according to the simplified Fick's Second Law by following equation:

$$D_{Li^+} = \frac{4}{\pi\tau}\left(\frac{m_B V_m}{M_B S}\right)^2 \left(\frac{\Delta E_s}{\Delta E_\tau}\right)^2$$

In the formula, m_B and M_B represent the mass and molecular weight of the active material respectively, V_m represents the molar volume, S represents the electrode surface area, τ represents the time of applying constant current, ΔE_s represents the change of steady-state voltage caused by one pulse, and ΔE_τ represents the change of voltage during the pulse.[11]

Supplementary Note 4

Hypothesizing that each transport step is a simple thermally activated process, that can raise the activation energies for Li$^+$ transport during these reactions from their Arrhenius behaviors by drawing log (R^{-1}) versus reciprocal temperature 1000/T plots[12]:

$$E_a = -19.144 \times slope \ (kJ \ mol^{-1})$$

Table S1. Comparison of the reported Si-based materials for LIBs.

Type of materials	Current density (A g^{-1})	Capacity (mA h g^{-1})	Capacity retention (%)
Si/SiO$_x$@C [S1]	0.5	1355	88% after 300 cycles
Si@SiO$_x$ [S2]	0.2	600	57% after 325 cycles
SiNPs-TMSPA-LCP [S3]	1	1000	55.6% after 300 cycles
Si@SiO$_x$/C [22]	1	823	93.4% after 350 cycles
C/VGSs@Si-C [S4]	1	1170	90.4% after 300 cycles
PCC-nSi[S5]	2	1046	88.7 after 400 cycles
Si@LM-SA@GO [S6]	2	660	67% after 300 cycles
Si@C [S7]	3	1080	85% after 200 cycles
Si-bPOD [S8]	3	1056	80% after 100 cycles
Si-C/VGSs/G[39]	5	363.1	76.8% after 3000 cycles
This work	**0.5**	**1689**	**96.6% after 300 cycles**
This work	**1**	**1506**	**90.2% after 300 cycles**
This work	**5**	**680**	**75.2% after 300 cycles**

References

S1. R.Maddipatla, C. Loka, K.S. Lee, ACS Appl. Mater. Interfaces, 2020, **12**, 54608-54618.

S2. S. Wang, Q. Wu, Z. Cai, Z. Ma, Z. Ahsan, Y. Li, Y. Ma, G. Song, W. Yang, C. Wen, ACS Appl. Energy Mater., 2023, **6** , 9788-9797.

S3. S. Pan, J. Han, Y. Wang, Z. Li, F. Chen, Y. Guo, Z. Han, K. Xiao, Yu, Z.; M. Yu, Adv. Mater., 2022, **34**, 2203617.

S4. M.Han, Y. Mu, L. Wei, L. Zeng, T. Zhao, Carbon Energy, 2024, **6**, e377.

S5. Q.Ma, Z. Zhao, Y. Zhao, H. Xie, P. Xing, D. Wang, H. Yin, Energy Storage Mater., 2021, **34**, 768-777.

S6. Y. Wang, H. Fan, L. Bai, J. Song, Y. Jin, S. Liu, W. Zheng, X. Xie, W. Liu, Chem. Eng. J., 2023, **452**, 139586.

S7. Q. Ma, H. Xie, J. Qu, Z. Zhao, B. Zhang, Q. Song, P. Xing, H. Yin, ACS Appl. Energy Mater., 2019, 3, 268-278.

S8. Y. Yu, C. Yang, Y. Jiang, J. Zhu, Y. Zhao, S. Liang, K. Wang, Y. Zhou, Y. Liu, J. Zhang, Small, 2023, **19**, 2303779.

S9. Z. Chen, X. Lu, Y. Zhang, Y. Kang, X. Jin, X. Zhang, Y. Li, H. Wang, W. Huang, Adv. Funct. Mater., 2024, 34, 2314176.

S10. L. Hu, M. Jin, Z. Zhang, H. Chen, F. Boorboor Ajdari, J. Song, Adv. Funct. Mater., 2022, **32**, 2111560.

S11. X. Gao, W. Lu, J. Xu, Nano Energy, 2021, **81**, 105591.

S12. P. Du, X. Fan, B. Zhang, L. Cao, J. Ren, X. Ou, X. Guo, Q. Liu, Energy Storage Mater., 2022, **50**, 648-657.